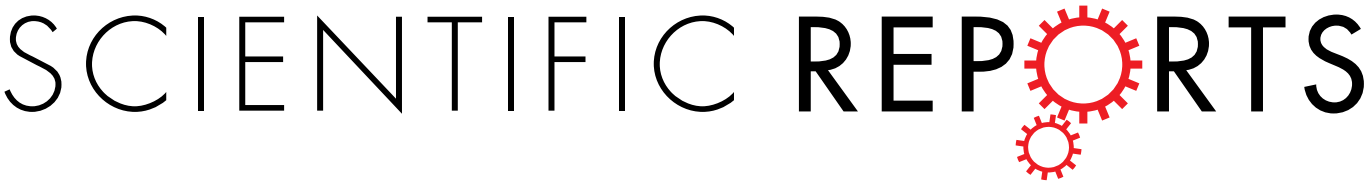

OPEN

Thickness Control of the Spin-Polarized Two-Dimensional Electron Gas in $LaAlO_3/BaTiO_3$ Superlattices

Received: 12 June 2017
Accepted: 18 December 2017
Published online: 11 January 2018

Chen Chen[1], Le Fang[2], Jihua Zhang[1,3], Guodong Zhao[1] & Wei Ren[1,2]

We explored the possibility of increasing the interfacial carrier quantum confinement, mobility and conductivity in the $(LaAlO_3)_n/(BaTiO_3)_n$ superlattices by thickness regulation using the first-principles electronic structure calculations. Through constructing two different interfacial types of $LaAlO_3/BaTiO_3$ superlattices, we discovered that the LaO/TiO_2 interface is preferred from cleavage energy consideration. We then studied the electronic characteristics of two-dimensional electron gas (2DEG) produced at the LaO/TiO_2 interface in the $LaAlO_3/BaTiO_3$ superlattices via spin-polarized density functional theory calculations. The charge carrier density of 2DEG has a magnitude of 10^{14} cm^{-2} (larger than the traditional system $LaAlO_3/SrTiO_3$), which is mainly provided by the interfacial Ti $3d_{xy}$ orbitals when the thicknesses of $LaAlO_3$ and $BaTiO_3$ layers are over 4.5 unit cells. We have also revealed the interfacial electronic characteristics of the $LaAlO_3/BaTiO_3$ system, by showing the completely spin-polarized 2DEG mostly confined at the superlattice interface. The interfacial charge carrier mobility and conductivity are found to be converged beyond the critical thickness. Therefore, we can regulate the interfacial confinement for the spin-polarized 2DEG and quantum transport properties in $LaAlO_3/BaTiO_3$ superlattice via controlling the thicknesses of the $LaAlO_3$ and $BaTiO_3$ layers.

Two-dimensional electron gas (2DEG) can be generated at the interface of heterojunction constructed by two insulating perovskite materials. The 2DEG has many unique electronic properties, such as ferroelectric polarization enhancement[1], high carrier mobility[2], two-dimension superconductivity[3], magnetism at the interface[4], electronic spin polarization[5,6], and so on. With the rapid development of thin film growth technology including molecular beam epitaxy[7], chemical vapor deposition[8], and pulsed laser deposition[9], the nature and functionalities of 2DEG draw great attention from both experimental and theoretical points of view.

Generally, there are two primary mechanisms to be involved in the formation of 2DEG at the heterojunction interface: oxygen vacancies[10] and electronic reconstruction[11]. A prominent experiment is $LaAlO_3/SrTiO_3$ system, in which the $LaAlO_3$ slab is grown on the $SrTiO_3$ substrate[12]. It is well known that a metallic phase is confined within several monolayers near the LaO/TiO_2 interface and therefore formed a 2DEG. The $LaAlO_3$ slab consists of alternating charged layers LaO and AlO_2, while the $SrTiO_3$ substrate can be considered a stack of alternating neutral layers SrO and TiO_2 along the (001) direction. The polarization discontinuity at the LaO/TiO_2 interface causes the electrostatic potential divergence. To avoid the polar discontinuity, half an electron is transferred from the charged layer LaO to the neutral layer TiO_2[11], resulting in a metallic phase at the interface of the $LaAlO_3/SrTiO_3$ system.

It is found that the 2DEG may even become magnetic at low temperature by Brinkman *et al.*[13], as generated at the LaO/TiO_2 interface between the non-magnetic $LaAlO_3$ and $SrTiO_3$ materials. This interesting phenomenon has the origin of the induced electrons exchange splitting in the Ti-3d orbital[14], which is confirmed by the first principles calculations with spin-polarization. Formation of the completely spin-polarized 2DEG is extremely promising for spintronics applications. From the previous work of Nazir *et al.*[15], $LaAlO_3/BaTiO_3$ model shows

[1]International Center for Quantum and Molecular Structures, Physics Department, Shanghai University, Shanghai, 200444, China. [2]Materials Genome Institute and Shanghai Key Laboratory of High Temperature Superconductors, Shanghai University, Shanghai, 200444, China. [3]Guizhou Provincial Key Laboratory of Computational Nano-Material Science, Guizhou Education University, Guiyang, 550018, China. Correspondence and requests for materials should be addressed to W.R. (email: renwei@shu.edu.cn)

higher interfacial charge carrier density, stronger quantum confinement, and larger magnetic moment than the previously reported $SrTiO_3$-based model superlattices. In this work, we carry out first principles calculations of the $LaAlO_3/BaTiO_3$ system with a special emphasis of oxide thickness control. As a matter of fact, previous experiments[16] of $LaAlO_3/BaTiO_3$ superlattices have been realized with 20 periodic numbers and varied stacking periodicity of 2/2 (2 unit cells $LaAlO_3$/2 unit cells $BaTiO_3$), 3/3, 4/4, 5/5 and 8/8.

$BaTiO_3$ is a tetragonal perovskite-type structure at the room temperature, when the temperature is above 393 K, the bulk $BaTiO_3$ changes from the tetragonal to cubic structure with a lattice constant of 4.012 Å[17], band gap of 3.2 eV[18], and Curie temperature of 415 K[19]. $LaAlO_3$ is the other building block for the $LaAlO_3/BaTiO_3$ model and it can be used as substrate for growing many lattice-mismatched perovskite materials. At room temperature, $LaAlO_3$ has a perovskite-like structure with a slight rhombohedral distortion, at high temperature $LaAlO_3$ also has the cubic perovskite structure with a lattice constant of 3.789 Å, band gap of 5.6 eV[12], and it has a lattice mismatch of 5.56% with $BaTiO_3$ material.

In this work, for the first-principles electronic structure calculations, we first build two kinds of $LaAlO_3/BaTiO_3$ superlattices with different interfaces. For example, in the $(LaAlO_3)_{4.5}/(BaTiO_3)_{4.5}$ superlattice, we find that the LaO/TiO_2 interface is the more preferential configuration due to its highest cleavage energy, compared with the BaO/AlO_2 interface[15,20–23]. Furthermore, we show that the $LaAlO_3/BaTiO_3$ superlattices with LaO/TiO_2 interface could produce the spin-polarized 2DEG, and the completely spin-polarized 2DEG is strongly confined at the interfacial TiO_2 layer when the thicknesses of $LaAlO_3$ and $BaTiO_3$ layers are both larger than 4.5 unit cells.

By means of the analysis of the layer-resolved partial density of states (DOS), we discovered that the mechanism for the spin-polarized 2DEG formation is similar to the $LaAlO_3/SrTiO_3$ systems[11]. Half an electron transfers from the LaO layer to the TiO_2 layer in the interface of non-stoichiometric $LaAlO_3/BaTiO_3$ superlattices, in which two symmetrical and identical LaO/TiO_2 interfaces are considered in the computation[24]. The spin-polarized 2DEG contributed by the interfacial Ti $3d_{xy}$ orbitals is found to be tightly confined at the interfacial TiO_2 monolayer, corresponding to the theoretically computed charge carrier density of $2.25 \times 10^{14}\,cm^{-2}$ in $LaAlO_3/BaTiO_3$ superlattice when the thicknesses of $LaAlO_3$ and $BaTiO_3$ are both greater than 4.5 unit cells. Whereas we constructed the superlattice $(SrTiO_3)_{4.5}/(LaAlO_3)_{4.5}$, the calculated two-dimensional electron gas density at the interface is $1.48 \times 10^{14}\,cm^{-2}$ (see Fig. S7 in Supplemental Information) which is significantly lower than our $LaAlO_3/BaTiO_3$ superlattice. In order to qualitatively analyze the effect of the thicknesses of $LaAlO_3$ and $BaTiO_3$ layers on the properties of interfacial transport characteristics, we calculated the relative interfacial charge carrier mobility and conductivity by using the $(LaAlO_3)_{2.5}/(BaTiO_3)_{2.5}$ superlattice as reference. Our results suggest that, when the thicknesses of $LaAlO_3$ and $BaTiO_3$ layers become larger than 4.5 unit cells, the mobility and conductivity are converged to the above-mentioned value. Therefore, our work gives theoretical guidance for generating superior spin-polarized 2DEG in $LaAlO_3/BaTiO_3$ superlattice, and enhancing the interfacial transport properties of the charge carrier through adjusting the thicknesses of $LaAlO_3$ and $BaTiO_3$ layers.

We also consider carefully the effect of ferroelectric $BaTiO_3$ on the $BaTiO_3/LaAlO_3$ superlattices. In detail, we constructed tetragonal $BaTiO_3$ with lattice constants $a = b = 3.9945$ Å and $c = 4.0335$ Å for the different $(LaAlO_3)_n/(BaTiO_3)_n$ superlattices ($n = 2.5$ to 8.5). Note that after relaxation the initial uniaxial ferroelectric structure transforms to two opposite polar modes pointing towards the bulk inside $BaTiO_3$ (see Fig. S1 in Supplemental Information), and a tiny residual polarization of about $2.9\,\mu C/cm^2$ which points toward the direction of initial ferroelectric polarization we set in the perovskite $BaTiO_3$. This means that our mirror symmetry is not exact and the superlattice presents a pseudo-ferroelectricity. In order to avoid the energy-consuming charged domain wall in the middle of $BaTiO_3$ the polarization diminishes (see Fig. S1). Two separate bands are found near the conduction band minima which were actually almost degenerate in the exact mirror-symmetric $BaTiO_3$ case (see Fig. S2 in Supplemental Information).

Results

Interface energetics. Periodic boundary conditions are applied when constructing $(LaAlO_3)_n/(BaTiO_3)_n$ superlattices along (001) direction[25], where n is the number of unit cells of $LaAlO_3$ and $BaTiO_3$ ($n = 2.5$ to 8.5)[26,27]. Both non-stoichiometric $LaAlO_3$ and $BaTiO_3$ slabs have two distinct kinds of terminal surfaces[28], the $LaAlO_3$ slab has LaO and AlO_2 terminal surface, while the $BaTiO_3$ substrate has BaO and TiO_2 terminal surface. Thus, we build two kinds of symmetric interface for $(LaAlO_3)_n/(BaTiO_3)_n$ superlattices, including LaO/TiO_2 or BaO/AlO_2 interfaces, as shown in Fig. 1. In the supercell we have two interfaces, namely the left/right side interface and the middle interface, respectively. The index n indicates the $LaAlO_3$ ($BaTiO_3$) unit cells counting from the middle interface location.

In order to compare the interface stability for these two types of interfaces, we introduced the cleavage energy[15,20–23] E_{cleav} which is defined as:

$$E_{cleav} = (E_{LAO} + E_{BTO} - E_S)/2A \quad (1)$$

where E_S is the total energy for the superlattices containing two kinds of perovskite compositions that are $LaAlO_3$ and $BaTiO_3$; E_{LAO} and E_{BTO} represent the energy of $LaAlO_3$ and $BaTiO_3$ slab systems, which have the same superlattice lattice constant with $LaAlO_3/BaTiO_3$ supercell, but $BaTiO_3$ or $LaAlO_3$ slabs are replaced by the vacuum of same size. The area of an interface in the superlattices is defined as A, and the factor of 2 in the formula indicates two symmetric interfaces in the superlattice models. The physical meaning of cleavage energy is the energy needed to decompose the $(LaAlO_3)_n/(BaTiO_3)_n$ superlattices into two sections, and thus, the numerical value of the cleavage energy determines the compactness of the interfacial cohesion between the $LaAlO_3$ and $BaTiO_3$ slabs, which can describe the thermodynamic stability of the interface[21,22,29].

We have calculated cleavage energy E_{cleav} for $(LaAlO_3)_n/(BaTiO_3)_n$ superlattices ($n = 2.5$ to 8.5) with LaO/TiO_2 and BaO/AlO_2 interfaces, as listed in Table 1. Overall, it can be found that cleavage energy of LaO/TiO_2 interface

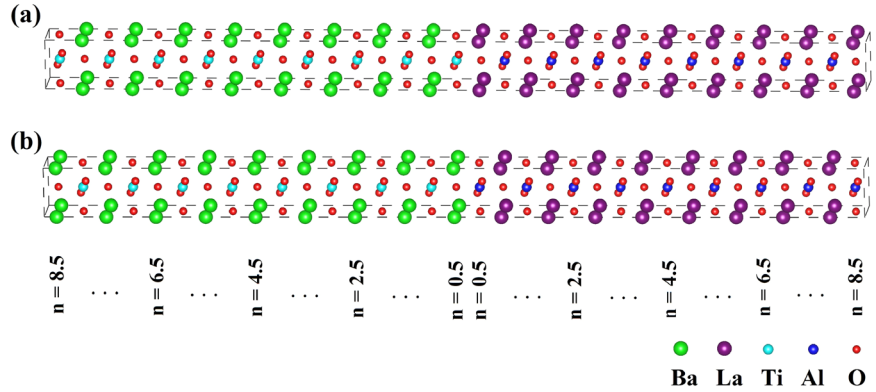

Figure 1. Atomic structures of the supercells with the (**a**) LaO/TiO_2, (**b**) BaO/AlO_2 interfaces in $(LaAlO_3)_{8.5}/(BaTiO_3)_{8.5}$ superlattice.

Systems	Cleavage energy (eV/Å^2)	
	LaO/TiO_2	BaO/AlO_2
$(LaAlO_3)_{2.5}/(BaTiO_3)_{2.5}$	0.189	0.117
$(LaAlO_3)_{3.5}/(BaTiO_3)_{3.5}$	0.175	0.109
$(LaAlO_3)_{4.5}/(BaTiO_3)_{4.5}$	0.164	0.101
$(LaAlO_3)_{5.5}/(BaTiO_3)_{5.5}$	0.155	0.092
$(LaAlO_3)_{6.5}/(BaTiO_3)_{6.5}$	0.147	0.083
$(LaAlO_3)_{7.5}/(BaTiO_3)_{7.5}$	0.138	0.074
$(LaAlO_3)_{8.5}/(BaTiO_3)_{8.5}$	0.127	0.066

Table 1. Calculated cleavage energy (eV/Å^2) for the $(LaAlO_3)_n/(BaTiO_3)_n$ superlattices (n = 2.5 to 8.5) with the LaO/TiO_2 and BaO/AlO_2 interfaces.

is higher than BaO/AlO_2 interface for the same index n. This means that the superlattices with LaO/TiO_2 interface are generally more stable than BaO/AlO_2 interface. With the increase of the parameter n, it is clearly noted that cleavage energy decreased from 0.117 eV/Å^2 to 0.066 eV/Å^2 for BaO/AlO_2 interface and decreased from 0.189 eV/Å^2 to 0.127 eV/Å^2 for LaO/TiO_2 interface. This suggests that with the increase of the superlattice size, the interface becomes less stable.

2DEG in $LaAlO_3/BaTiO_3$ superlattices. To investigate the interface type induced electronic properties modification for the $(LaAlO_3)_n/(BaTiO_3)_n$ superlattices, we calculated the total DOS for the LaO/TiO_2 and BaO/AlO_2 interfaces for $(LaAlO_3)_n/(BaTiO_3)_n$ superlattices (n = 2.5, 4.5, 6.5, and 8.5), as shown in Fig. 2. It can be seen that spin-polarized 2DEG is generated in the superlattices with LaO/TiO_2 interface. Like the classical model $LaAlO_3/SrTiO_3$, spin-polarized 2DEG is seen at the LaO/TiO_2 interface, as reported by Nazir *et al.*[30]. Making 2DEG spin-polarized is a very important for spintronics applications, where the regulation the atomic layer types at the interface enlarges the spectrum of potential applications. Experimental scientists can control the interface types by inserting atomic layers, using feasible and widely applied techniques. For example, Yajima *et al.* successfully controlled the $SrRuO_3/Nb:SrTiO_3$ Schottky heterojunction by inserting an artificial interface dipole[31], and Chen *et al.* enhanced the mobility of 2DEG through inserting a single-unit-cell layer of $La_{1-x}Sr_xMnO_3$ at the interface[32]. Inspection of Fig. 2 indicated that the electronic states in the model LaO/TiO_2 are half-metallic and do not change much in the energy range from −1.4 eV to Fermi level when the index $n \geq 4.5$.

It is important to reveal the origin of spin-polarized 2DEG in superlattices (n = 2.5 to 8.5), we thus plot the layer-resolved partial DOS along with the spin charge density for $(LaAlO_3)_{2.5}/(BaTiO_3)_{2.5}$ superlattice, as shown in Fig. 3(a). We use IF-1, IF-3, IF-5, and IF-7 to represent the first, third, fifth, and seventh TiO_2 monolayers. The 2DEG originates from Ti 3d states in the IF-1 and IF-3 TiO_2 monolayers, while the $LaAlO_3$ slab does not contribute to the 2DEG in the $(LaAlO_3)_{2.5}/(BaTiO_3)_{2.5}$ superlattice, demonstrating that the electrons provided by LaO monolayer are shared by Ti atoms in all TiO_2 layers. In other words, the spin-polarized 2DEG may diffuse from the interface to the inside of the $BaTiO_3$. The orbital-resolved partial DOS figures, as shown in Fig. 3(b), suggest that the half-metallic states at IF-1 TiO_2 monolayer are mostly from Ti $3d_{xy}$ orbitals, Ti $3d_{yz}$ orbitals and Ti $3d_{xz}$ orbitals only give a little contribution. While at IF-3 TiO_2 monolayer, different from IF-1, most of the half-metallic states come from Ti $3d_{yz}$ orbitals, partially from Ti $3d_{xz}$ orbital and none from Ti $3d_{xy}$ orbital.

Now let us look at the distribution of the 2DEG and the contribution of Ti atomic orbitals as the thickness parameter n increases, hence the layer-resolved partial DOS along with the spin charge density for $(LaAlO_3)_{6.5}/(BaTiO_3)_{6.5}$ superlattice is shown in Fig. 4(a). It is noted that nearly all the half-metallic states are contributed by the interfacial TiO_2 monolayer, and the contributions from the IF-3, IF-5, and IF-7 TiO_2 layer are negligible. This clearly indicates that the spin-polarized 2DEG is tightly confined at the interfacial TiO_2 layer.

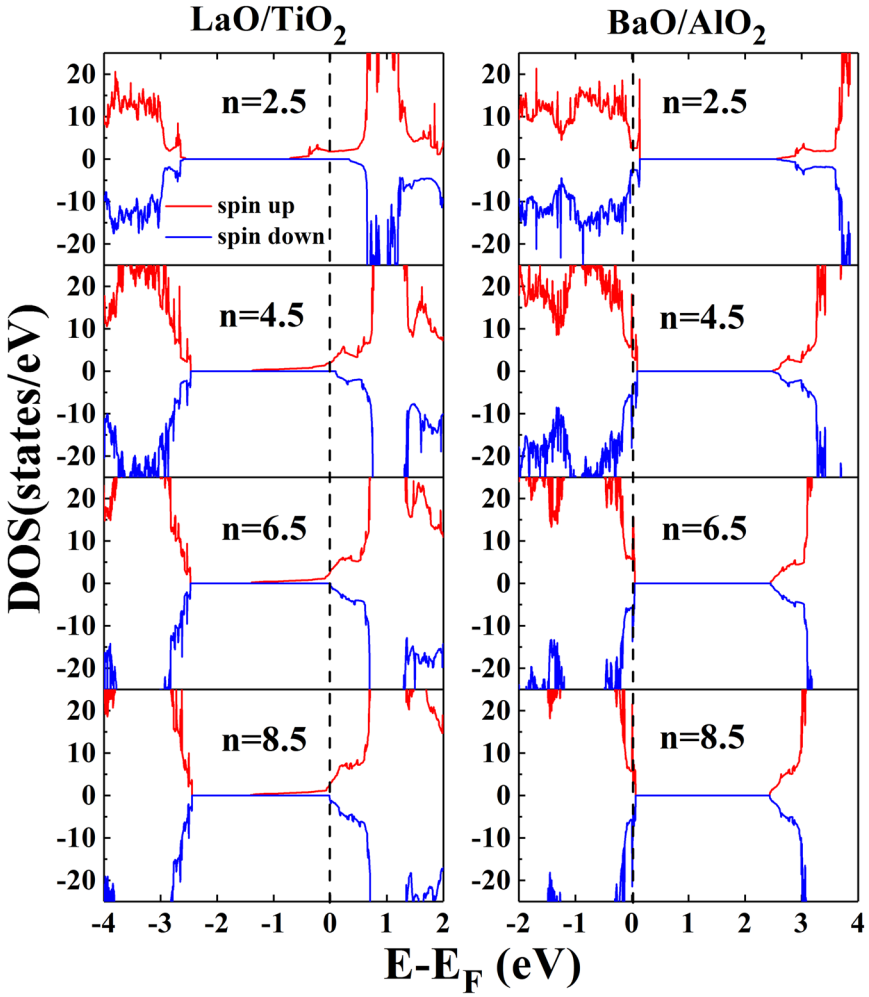

Figure 2. Calculated spin-resolved total density of states (DOS) for the $(LaAlO_3)_n/(BaTiO_3)_n$ superlattices (n = 2.5, 4.5, 6.5, and 8.5) with the LaO/TiO_2 (left column) and BaO/AlO_2 (right column) interfaces. The red and blue lines show the majority-spin and minority-spin, respectively. The vertical lines at 0 eV indicate the Fermi level in all DOS plots.

The mechanism for 2DEG formation is similar to the $LaAlO_3/SrTiO_3$ systems, in the $(LaAlO_3)_n/(BaTiO_3)_n$ superlattices (n = 2.5 to 8.5) with LaO/TiO_2 interface, an "extra" electron is injected into the supperlattice as a result of an electron located at the additional LaO layer[24]. In order to analyze the contribution of the Ti 3d orbitals to the 2DEG, we plot the orbital-resolved partial DOS in Fig. 4(b). The spin-polarized 2DEG located at IF-1 TiO_2 monolayer is entirely contributed by Ti $3d_{xy}$ orbitals, and there is no obvious 2DEG in other TiO_2 monolayers near the Fermi level. Briefly, we find that the spin-polarized 2DEG is tightly confined at the interfacial TiO_2 monolayer in $(LaAlO_3)_{6.5}/(BaTiO_3)_{6.5}$ superlattice, and completely provided by the interfacial Ti $3d_{xy}$ orbitals. Through a comparison of the superlattices with thickness n = 2.5 and n = 6.5, the results show that the electronic property has a strong dependence on the superlattice size. Such tightly confined 2DEG at the interfacial TiO_2 monolayer, contributed by the Ti 3d states, is very consistent with the results of Nazir *et al.*[15]. Moreover, we have also find the difference of Ti 3d orbitals contribution to the DOS located near the interface when the period of superlattice is as short as n = 2.5.

Interfacial charge carrier density. Next, we calculated the interfacial charge carrier density[21,28,33,34] for the superlattices via integrating the partial DOS near the Fermi level of the occupied Ti 3d orbitals located at the interfacial TiO_2 monolayer[21,29], and displayed the relation between the interfacial charge carrier density and the parameter n, as shown in Fig. 5 (black line). When $n \leq 4.5$, the interfacial charge carrier density increased from $1.13 \times 10^{14}\,cm^{-2}$ to $2.25 \times 10^{14}\,cm^{-2}$ with the increase of the index n, when $n \geq 4.5$, the interfacial charge carrier density was converged to $2.25 \times 10^{14}\,cm^{-2}$. From the work of Meevasana *et al.*[35], the 2DEG with the electron density was measured to be as large as $8 \times 10^{13}\,cm^{-2}$, formed at the bare $SrTiO_3$ surface in $LaAlO_3/SrTiO_3$ system. We also constructed the $(SrTiO_3)_{4.5}/(LaAlO_3)_{4.5}$ superlattice and found the 2DEG density at the interface is $1.48 \times 10^{14}\,cm^{-2}$. We plot the layer-resolved partial DOS for $(SrTiO_3)_{4.5}/(LaAlO_3)_{4.5}$ superlattice, as shown in the Fig. S7. By comparison, the system we studied can form a 2DEG with even higher charge carrier density than the traditional $LaAlO_3/SrTiO_3$ systems[15]. For $LaAlO_3/SrTiO_3$ superlattice we found that there is more electron density

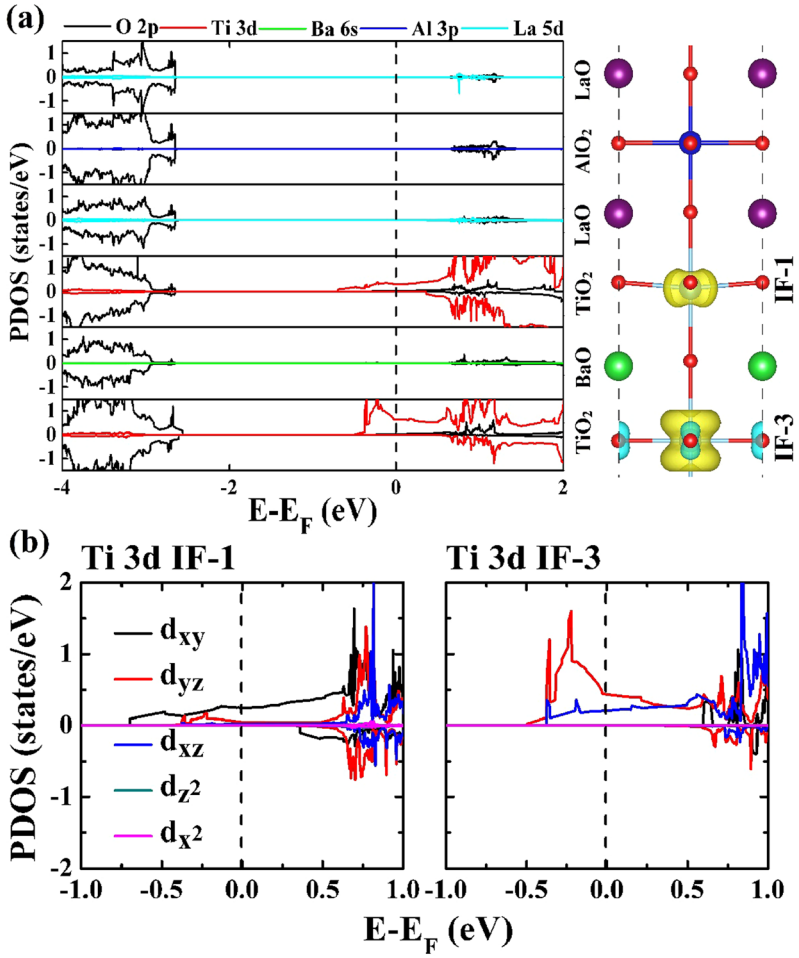

Figure 3. (**a**) Calculated layer-resolved partial DOS for the $(LaAlO_3)_{2.5}/(BaTiO_3)_{2.5}$ superlattice in the range from −4.0 to 2.0 eV, with the spin density corresponding to each of the oxide monolayers. (**b**) The orbital-resolved partial DOS for Ti atom at the first (IF-1) and the third (IF-3) TiO_2 monolayers.

penetrating into the $SrTiO_3$ near the interface. This explains why we could obtain a higher electron density of $LaAlO_3/BaTiO_3$ superlattice than that of $LaAlO_3/SrTiO_3$ superlattice.

In order to ensure the reliability of the relationship between interfacial charge carrier density and the parameter n, we also calculated local magnetic moment[29,33,36] on Ti atoms of the interfacial TiO_2 monolayer. From Fig. 5 (red line), we observe that the magnetic moment versus n shows a similar trend with the relationship between the interfacial charge carrier density and the parameter n. The Ti atomic magnetic moment increased from 0.24 μ_B to 0.42 μ_B with the increase of the parameter n, and then converged to 0.42 μ_B when the thicknesses of $LaAlO_3$ and $BaTiO_3$ layers are greater than 4.5 unit cells. Similar to $LaAlO_3/SrTiO_3$ systems, for the $(LaAlO_3)_n/(BaTiO_3)_n$ superlattices, about half electron is transferred from addition LaO monolayer to the neighboring TiO_2 monolayer in the interface as a result of the polar discontinuity, the half-electron will occupy partial Ti 3d orbitals[37], and our saturation value result is very close to 0.46 μ_B reported by Nazir *et al.*[15].

Calculation of electron effective mass. To further discuss the effect of superlattice size on electronic properties of the 2DEG, we calculated the band structure along the path M-Γ-X of the Brillouin zone[21,22,38], as shown in Fig. 6. We can see that there is only majority-spin electrons pass through the Fermi level, resulting in the spin-polarized 2DEG at the superlattice interface. Figure 6 also suggested that the bottom conduction band becomes deeper in energy as the parameter n increases. Moreover, such band consists two degenerate energy levels and splits into two bands when n = 8.5. The degenerate states are due to the fact that there are two identical interfaces in the superlattice, whereas a slight symmetry breaking in the superlattice structure may result in the degenerate level splitting. Through the above DOS analysis, we realize that the conduction band passing through the Fermi level is provided by the Ti 3d orbitals, mainly supplied by Ti $3d_{xy}$ state.

It is important to qualitatively compare the interfacial electron transport characteristics in the $(LaAlO_3)_n/(BaTiO_3)_n$ superlattices. We calculated the electron relative effective masses (m^*/m_e) along the Γ-X and Γ-M directions using the bottom conduction band for each superlattice, in which m_e is the electron mass, and the results are listed in Table 2. The calculated electron effective masses are obtained from the following formula[20–22,38]:

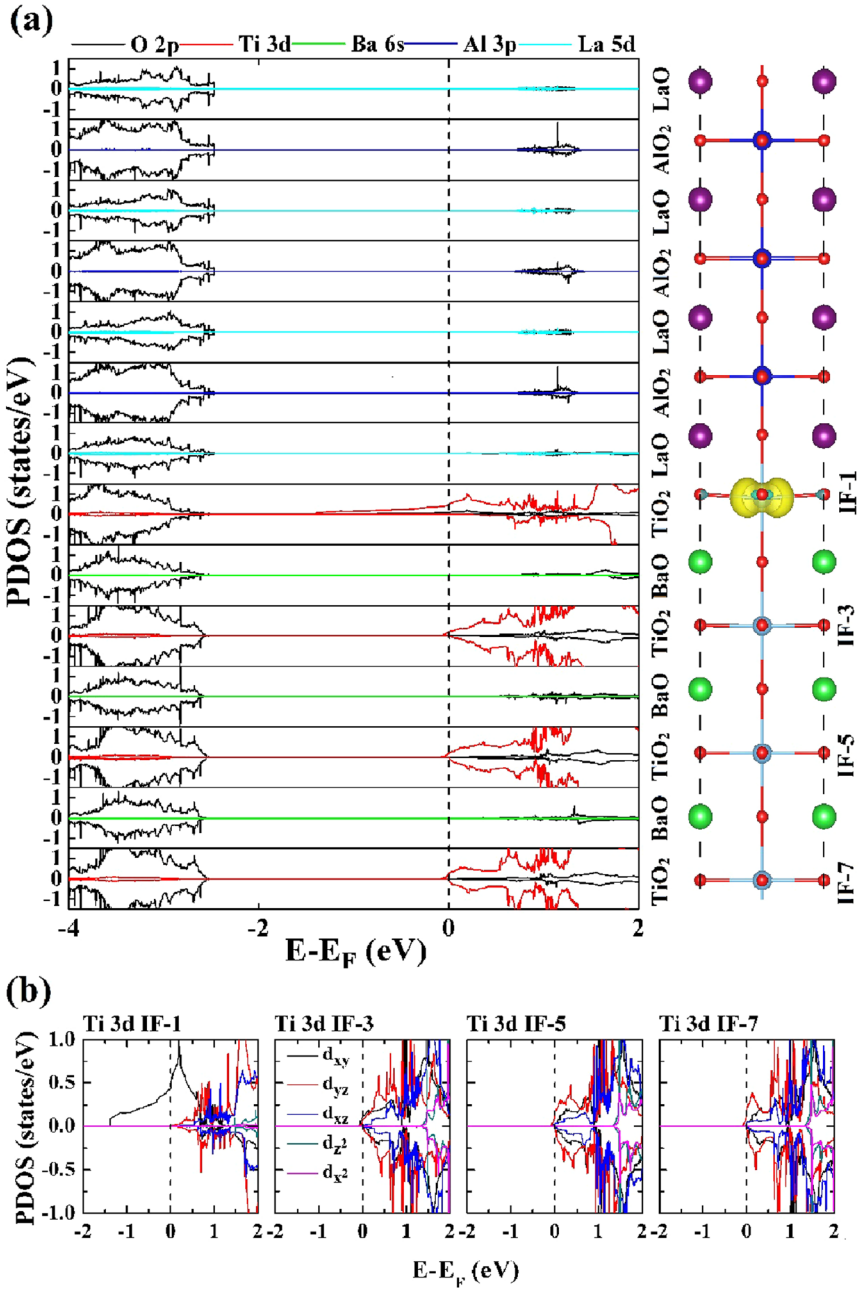

Figure 4. (**a**) Calculated layer-resolved partial DOS for $(LaAlO_3)_{6.5}/(BaTiO_3)_{6.5}$ model in the range from −4.0 to 2.0 eV, together with the spin density projected on to each of the oxide monolayers. (**b**) The orbital-resolved DOS for Ti atom at the first (IF-1), third (IF-3), fifth (IF-5), and seventh (IF-7) TiO_2 monolayers, respectively.

$$\frac{1}{m^*} = \frac{1}{\hbar^2}\frac{\partial^2 E_{CB}}{\partial k^2} \tag{2}$$

where ħ is the reduced Planck constant, E_{CB} and k are the energy and wavevector of the bottom conduction band, respectively. From the Table 2 we can clearly find that the relative effective masses, whether along the Γ-X or Γ-M direction, decreased from 0.351 to 0.273 with the increase of the parameter n. When $n \geq 4.5$, the m^*/m_e is converged to 0.273, suggesting that the relative effective mass of the 2DEG becomes a constant. We can also find almost no difference between the two kinds of relative effective mass, indicating same characteristics along the two transport directions for the 2DEG. In the typical $LaAlO_3/SrTiO_3$ systems, the relative effective mass of the 2DEG confined at $SrTiO_3$ surface is 0.5–0.6 measured by the angle-resolved photoemission spectroscopy from the report of Meevasana *et al.*[35]. Therefore our studied 2DEG has a smaller effective mass, and thus better carrier mobility than the $LaAlO_3/SrTiO_3$ systems.

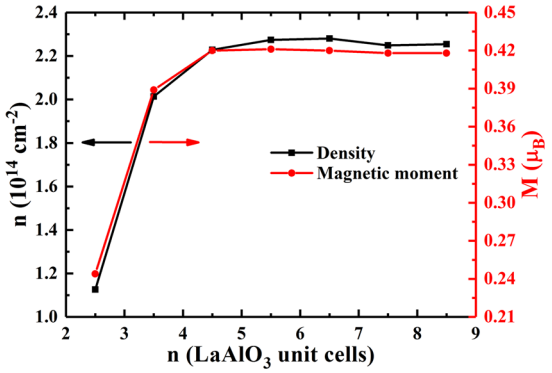

Figure 5. Calculated interfacial charge carrier density for $(LaAlO_3)_n/(BaTiO_3)_n$ superlattices (n = 2.5 to 8.5) with LaO/TiO_2 interface and the magnetic moment of the Ti atom at the interface as a function of the index n.

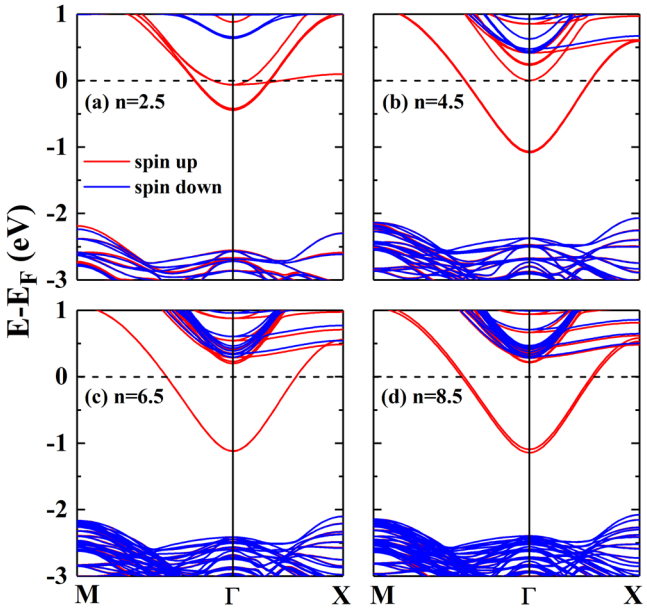

Figure 6. Electronic band structures for the (**a**) n = 2.5, (**b**) n = 4.5, (**c**) n = 6.5, and (**d**) n = 8.5 $(LaAlO_3)_n/(BaTiO_3)_n$ superlattices, respectively. The red (blue) lines show the majority (minority)-spin sates, and the black horizontal dashed line at 0 eV indicates the Fermi level. The bottom conduction band is employed to calculate the relative electron effective mass.

	m*/m$_e$	
Systems	Γ-X	Γ-M
$(LaAlO_3)_{2.5}/(BaTiO_3)_{2.5}$	0.351	0.351
$(LaAlO_3)_{3.5}/(BaTiO_3)_{3.5}$	0.285	0.285
$(LaAlO_3)_{4.5}/(BaTiO_3)_{4.5}$	0.273	0.273
$(LaAlO_3)_{5.5}/(BaTiO_3)_{5.5}$	0.273	0.274
$(LaAlO_3)_{6.5}/(BaTiO_3)_{6.5}$	0.273	0.274
$(LaAlO_3)_{7.5}/(BaTiO_3)_{7.5}$	0.274	0.275
$(LaAlO_3)_{8.5}/(BaTiO_3)_{8.5}$	0.274	0.274

Table 2. Calculated relative electron effective mass m*/m$_e$ along the Γ-X and Γ-M paths for the $(LaAlO_3)_n/(BaTiO_3)_n$ superlattices.

When considering the ferroelectricity of $BaTiO_3$ in $(LaAlO_3)_n/(BaTiO_3)_n$ superlattices (n = 2.5, 4.5, 6.5, and 8.5), by observing the change of its properties, two separate bands are found near the conduction band minima

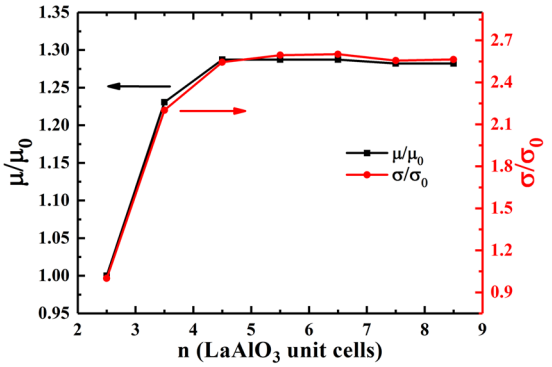

Figure 7. Calculated relative interfacial electron mobility (μ/μ_0) and electrical conductivity (σ/σ_0) for the $(LaAlO_3)_n/(BaTiO_3)_n$ superlattices, where the μ_0 and σ_0 representative the interfacial electron mobility and electrical conductivity for the $(LaAlO_3)_{2.5}/(BaTiO_3)_{2.5}$ reference system, respectively.

which were actually almost degenerate in the exact mirror-symmetric $BaTiO_3$ case (see Figs S2–4 in Supplemental Information and Fig. 6). This shows that the two interfaces will exhibit different electronic band structure characteristics when $BaTiO_3$ is in ferroelectric state.

Charge carrier mobility and conductivity. Now let us compare the interfacial electron mobility and conductivity in the $(LaAlO_3)_n/(BaTiO_3)_n$ superlattices. For that, we calculated the relative interfacial electron mobility (μ/μ_0) and electrical conductivity (σ/σ_0)[21,22,38,39] with respect to $(LaAlO_3)_{2.5}/(BaTiO_3)_{2.5}$ superlattice, and plotted the results as function of the index n, as shown in Fig. 7. We employed the following formulas:

$$\mu = e\langle\tau\rangle/m^* \quad (3)$$

$$\sigma = ne\mu \quad (4)$$

where e, $\langle\tau\rangle$, m*, n, μ, and σ represent elemental charge, average scattering time, effective mass, charge carrier density, carrier mobility, and electrical conductivity, respectively. The scattering time $\langle\tau\rangle$ is assumed to be a constant[40], determined by several scattering factors such as phonon scattering, electron-electron scattering, impurity scattering, and so on[41,42]. Our results show that, when the thicknesses of $LaAlO_3$ and $BaTiO_3$ layers are greater than 4.5 unit cells, the superlattices have a high and saturated carrier mobility and conductivity. Interestingly, the carrier conductivity for superlattices with $n \geq 4.5$ is about 2.6 times than the reference superlattice, which is consistent with the results of the interfacial charge carrier density and the relative charge carrier effective mass. These results show that we can obtain a spin-polarized 2DEG by regulating the thicknesses of $LaAlO_3$ and $BaTiO_3$ layers in the process of growing $LaAlO_3/BaTiO_3$ superlattices.

Conclusion

In summary, spin-polarized density functional theory calculations are employed to investigate the possibility of enhancing the 2DEG quantum confinement at LaO/TiO_2 interface and the interfacial charge carrier density, mobility, and conductivity in $LaAlO_3/BaTiO_3$ superlattice by using thickness control. We find that the superlattices with LaO/TiO_2 interface are more stable than BaO/AlO_2 from the cleavage energy calculations. When the critical thicknesses of $LaAlO_3$ and $BaTiO_3$ layers are over 4.5 unit cells, the spin-polarized 2DEG is mainly provided by the interfacial Ti $3d_{xy}$ orbitals and completely confined at the interface. In such cases, through the study of the interfacial charge carrier density, mobility, and conductivity, we confirm that these properties become independent of the thickness. Our present work provides theoretical understanding to produce and enhance the interfacial quantum confinement for spin-polarized 2DEG and the interfacial transport properties by adjusting the thicknesses of $LaAlO_3$ and $BaTiO_3$ layers. In $LaAlO_3/BaTiO_3$ superlattice, electrons are almost bound at the interfaces, but for $LaAlO_3/SrTiO_3$ superlattice we found that there is electron density penetrating into the $SrTiO_3$ near the interface.

Computational and Structural Details. In this study, for all density functional theory (DFT)[43] calculations we used Vienna Ab initio Simulation Package(VASP)[44]. The electron exchange-correlation interaction was described by the generalized gradient approximation (GGA) parametrized by the Perdew-Burke-Ernzerhof (PBE) plus the on-site Coulomb interaction approach (GGA + U)[45]. The projected augmented method (PAW) was used to describe the electron-ion interaction. In order to more accurately describe the electronic states of strongly correlated electrons, effective U value of 5.8 eV and 7.5 eV were applied to Ti 3d and La 4 f orbitals[46,47], respectively. Such U values are well tested and more results are in Figs S5–6 of the Supplemental Information. Our calculations were performed by employing a cutoff energy of 450 eV for the plane wave basis set and a Monkhorst-Pack k-point mesh of $6 \times 6 \times 1$ (except for $n = 2.5$ we use $6 \times 6 \times 2$). The convergence of electronic energy was set to 10^{-6} eV in the self-consistent calculations. The atomic positions were optimized to simulate the epitaxial superlattice until the interatomic forces were small than 0.03 eV/Å.

We used slab model to build $(LaAlO_3)_n/(BaTiO_3)_n$ superlattices (n = 2.5 to 8.5) by staking the epitaxial slabs using $BaTiO_3$ lattice parameters, in which n is a half-integer representing the number of $LaAlO_3$ and $BaTiO_3$ unit cells along (001) direction. We have constructed two types of superlattices interface, namely LaO/TiO_2 and BaO/AlO_2 interfaces. To simulate the epitaxial film growth in the experiment, we fixed the lattice constants in the ab-plane, and fully relaxed all atoms (unless otherwise stated) in the $LaAlO_3/BaTiO_3$ perovskite superlattices.

References

1. Neaton, J. B. & Rabe, K. M. Theory of Polarization Enhancement in Epitaxial $BaTiO_3/SrTiO_3$ Superlattices. *Appl. Phys. Lett.* **82**, 1586–1588, https://doi.org/10.1063/1.1559651 (2003).
2. Thiel, S., Hammerl, G., Schmehl, A., Schneider, C. W. & Mannhart, J. Tunable Quasi-Two-Dimensional Electron Gases in Oxide Heterostructures. *Science* **313**, 1942–1945, https://doi.org/10.1126/science.1131091 (2006).
3. Reyren, N. *et al*. Superconducting Interfaces Between Insulating Oxides. *Science* **317**, 1196–1199, https://doi.org/10.1126/science.1146006 (2007).
4. Weston, L., Cui, X. Y., Ringer, S. P. & Stampfl, C. Density-Functional Prediction of a Surface Magnetic Phase in $SrTiO_3/LaAlO_3$ Heterostructures Induced by Al Vacancies. *Phys. Rev. Lett.* **113**, 186401, https://doi.org/10.1103/PhysRevLett.113.186401 (2014).
5. Pentcheva, R. & Pickett, W. E. Avoiding the Polarization Catastrophe in $LaAlO_3$ Overlayers on $SrTiO_3$(001) Through Polar Distortion. *Phys. Rev. Lett.* **102**, 107602, https://doi.org/10.1103/PhysRevLett.102.107602 (2009).
6. Fredrickson, K. D. & Demkov, A. A. Switchable Conductivity at the Ferroelectric Interface: Nonpolar Oxides. *Phys. Rev. B* **91**, 115126, https://doi.org/10.1103/PhysRevB.91.115126 (2015).
7. Cho, A. Y. & Arthur, J. Molecular Beam Epitaxy. *Prog. Solid State Chem.* **10**, 157–191 (1975).
8. Park, J.-H. & Sudarshan, T. *Chemical Vapor Deposition*. Vol. 2 (ASM international, 2001).
9. Singh, R. K. & Narayan, J. Pulsed-Laser Evaporation Technique for Deposition of Thin Films: Physics and Theoretical Model. *Phys. Rev. B* **41**, 8843–8859, https://doi.org/10.1103/PhysRevB.41.8843 (1990).
10. Siemons, W. *et al*. Origin of Charge Density at $LaAlO_3$ on $SrTiO_3$ Heterointerfaces: Possibility of Intrinsic Doping. *Phys. Rev. Lett.* **98**, 196802, https://doi.org/10.1103/PhysRevLett.98.196802 (2007).
11. Nakagawa, N., Hwang, H. Y. & Muller, D. A. Why some interfaces cannot be sharp. *Nat. Mater.* **5**, 204–209, https://doi.org/10.1038/nmat1569 (2006).
12. Ohtomo, A. & Hwang, H. Y. A high-Mobility Electron Gas at the $LaAlO_3/SrTiO_3$ Heterointerface. *Nature* **427**, 423–426, https://doi.org/10.1038/nature02308 (2004).
13. Brinkman, A. *et al*. Magnetic Effects at the Interface Between Non-Magnetic Oxides. *Nat. Mater.* **6**, 493–496, https://doi.org/10.1038/nmat1931 (2007).
14. Pavlenko, N., Kopp, T., Tsymbal, E. Y., Sawatzky, G. A. & Mannhart, J. Magnetic and Superconducting Phases at the $LaAlO_3/SrTiO_3$ Interface: The Role of Interfacial Ti 3d Electrons. *Phys. Rev. B* **85**, https://doi.org/10.1103/PhysRevB.85.020407 (2012).
15. Nazir, S., Behtash, M. & Yang, K. S. Towards Enhancing Two-Dimensional Electron Gas Quantum Confinement Effects in Perovskite Oxide Heterostructures. *J. Appl. Phys.* **117**, 115305, https://doi.org/10.1063/1.4915950 (2015).
16. Li, Y., Hao, L., Deng, H., Chen, F. & Li, Y. Ferroelectric Properties of $LaAlO_3/BaTiO_3$ Superlattices Prepared by Laser Molecular-beam Epitaxy. *J. Appl. Phys.* **97**, 094103, https://doi.org/10.1063/1.1887829 (2005).
17. Miyake, S. & Ueda, R. On Phase Transformation of $BaTiO_3$. *J. Phys. Soc. Jpn.* **2**, 93–97, https://doi.org/10.1143/JPSJ.2.93 (1947).
18. Wemple, S. H. Polarization Fluctuations and the Optical-Absorption Edge in $BaTiO_3$. *Phys. Rev. B* **2**, 2679–2689, https://doi.org/10.1103/PhysRevB.2.2679 (1970).
19. Zalar, B., Laguta, V. V. & Blinc, R. NMR Evidence for the Coexistence of Crder-Disorder and Displacive Components in Barium Titanate. *Phys. Rev. Lett.* **90**, 037601, https://doi.org/10.1103/PhysRevLett.90.037601 (2003).
20. Fu, Y. T. & Heinz, H. Cleavage Energy of Alkylammonium-Modified Montmorillonite and Relation to Exfoliation in Nanocomposites: Influence of Cation Density, Head Group Structure, and Chain Length. *Chem. Mater.* **22**, 1595–1605, https://doi.org/10.1021/cm902784r (2010).
21. Wang, Y., Tang, W., Cheng, J., Behtash, M. & Yang, K. Creating Two-Dimensional Electron Gas in Polar/Polar Perovskite Oxide Heterostructures: First-Principles Characterization of $LaAlO_3/A^+B^{5+}O_3$. *ACS Appl. Mater. Interfaces* **8**, 13659–13668, https://doi.org/10.1021/acsami.6b02399 (2016).
22. Wang, Y., Tang, W., Cheng, J., Nazir, S. & Yang, K. High-Mobility Two-Dimensional Electron Gas in $SrGeO_3$- and $BaSnO_3$-Based Perovskite Oxide Heterostructures: an Ab initio Study. *Phys. Chem. Chem. Phys.* **18**, 31924–31929, https://doi.org/10.1039/c6cp05572a (2016).
23. Yin, L., Mi, W. & Wang, X. Ferroelectric Metal in Tetragonal $BiCoO_3/BiFeO_3$ Bilayers and Its Electric Field Effect. *Sci. Rep.* **6**, 20591, https://doi.org/10.1038/srep20591 (2016).
24. Wang, Y. *et al*. Prediction of a Spin-Polarized Two-Dimensional Electron Gas at the $LaAlO_3$/EuO(001) Interface. *Phys. Rev. B* **79**, https://doi.org/10.1103/PhysRevB.79.212408 (2009).
25. Chen, H., Kolpak, A. M. & Ismail-Beigi, S. Electronic and Magnetic Properties of $SrTiO_3/LaAlO_3$ Interfaces from First Principles. *Adv. Mater.* **22**, 2881–2899, https://doi.org/10.1002/adma.200903800 (2010).
26. Burton, J. D. & Tsymbal, E. Y. Prediction of Electrically Induced Magnetic Reconstruction at the Manganite/Ferroelectric Interface. *Phys. Rev. B* **80**, 174406, https://doi.org/10.1103/PhysRevB.80.174406 (2009).
27. Burton, J. D. & Tsymbal, E. Y. Giant Tunneling Electroresistance Effect Driven by an Electrically Controlled Spin Valve at a Complex Oxide Interface. *Phys. Rev. Lett.* **106**, 157203, https://doi.org/10.1103/PhysRevLett.106.157203 (2011).
28. Nazir, S., Cheng, J. & Yang, K. Creating Two-Dimensional Electron Gas in Nonpolar/Nonpolar Oxide Interface via Polarization Discontinuity: First-Principles Analysis of $CaZrO_3/SrTiO_3$ Heterostructure. *ACS Appl. Mater. Interfaces* **8**, 390–399, https://doi.org/10.1021/acsami.5b09107 (2016).
29. Nazir, S., Cheng, J., Behtash, M., Luo, J. & Yang, K. Interface Energetics and Charge Carrier Density Amplification by Sn-Doping in $LaAlO_3/SrTiO_3$ Heterostructure. *ACS Appl. Mater. Interfaces* **7**, 14294–14302, https://doi.org/10.1021/acsami.5b02770 (2015).
30. Nazir, S., Bernal, C. & Yang, K. Modulated Two-Dimensional Charge-Carrier Density in LaTiO3-Layer-Doped $LaAlO_3/SrTiO_3$ Heterostructure. *ACS Appl. Mater. Interfaces* **7**, 5305–5311, https://doi.org/10.1021/am508662q (2015).
31. Yajima, T. *et al*. Controlling Band Alignments by Artificial Interface Dipoles at Perovskite Heterointerfaces. *Nat. Commun.* **6**, 6759, https://doi.org/10.1038/ncomms7759 (2015).
32. Chen, Y. Z. *et al*. Extreme Mobility Enhancement of Two-Dimensional Electron Gases at Oxide Interfaces by Charge-Transfer-Induced Modulation Doping. *Nat. Mater.* **14**, 801–806, https://doi.org/10.1038/nmat4303 (2015).
33. Nazir, S. & Yang, K. First-Principles Characterization of the Critical Thickness for Forming Metallic States in Strained $LaAlO_3/SrTiO_3$(001) Heterostructure. *ACS Appl. Mater. Interfaces* **6**, 22351–22358, https://doi.org/10.1021/am506336w (2014).
34. Cheng, J., Nazir, S. & Yang, K. First-Principles Prediction of Two-Dimensional Electron Gas Driven by Polarization Discontinuity in Nonpolar/Nonpolar AHfO3/SrTiO3 (A = Ca, Sr, and Ba) Heterostructures. *ACS Appl. Mater. Interfaces* **8**, 31959–31967, https://doi.org/10.1021/acsami.6b06907 (2016).
35. Meevasana, W. *et al*. Creation and Control of a Two-Dimensional Electron Liquid at the Bare $SrTiO_3$ Surface. *Nat. Mater.* **10**, 114–118, https://doi.org/10.1038/nmat2943 (2011).

36. Wang, F. *et al*. Interfacial Multiferroics of TiO_2/$PbTiO_3$ Heterostructure Driven by Ferroelectric Polarization Discontinuity. *ACS Appl. Mater. Interfaces* **9**, 1899–1906, https://doi.org/10.1021/acsami.6b13183 (2017).
37. Burton, J. D. & Tsymbal, E. Y. Highly Spin-Polarized Conducting State at the Interface Between Nonmagnetic Band Insulators: $LaAlO_3$/FeS_2 (001). *Phys. Rev. Lett.* **107**, 166601, https://doi.org/10.1103/PhysRevLett.107.166601 (2011).
38. Cheng, J., Luo, J. & Yang, K. Comparison Studies of Interfacial Electronic and Energetic Properties of $LaAlO_3$/TiO_2 and TiO_2/$LaAlO_3$ Heterostructures from First-Principles Calculations. *ACS Appl. Mater. Interfaces* **9**, 7682–7690, https://doi.org/10.1021/acsami.6b12254 (2017).
39. Chen, Y. *et al*. Creation of High Mobility Two-Dimensional Electron Gases via Strain Induced Polarization at an Otherwise Nonpolar Complex Oxide Interface. *Nano Lett.* **15**, 1849–1854, https://doi.org/10.1021/nl504622w (2015).
40. Allen, P. B., Pickett, W. E. & Krakauer, H. Anisotropic Normal-State Transport Properties Predicted and Analyzed for High-Tcoxide Superconductors. *Phys. Rev. B* **37**, 7482–7490, https://doi.org/10.1103/PhysRevB.37.7482 (1988).
41. Peter, Y. & Cardona, M. *Fundamentals of Semiconductors: Physics and Materials Properties*. (Springer Science & Business Media, 2010).
42. Karamargin, M. C., Reynolds, C. A., Lipschultz, F. P. & Klemens, P. G. Lattice Thermal Conductivity and Deviations from Matthiessen's Rule for Dilute Alloys of Tin with Cadmium. *Phys. Rev. B* **6**, 3624–3633, https://doi.org/10.1103/PhysRevB.6.3624 (1972).
43. Hohenberg, P. & Kohn, W. Inhomogeneous Electron Gas. *Phys. Rev.* **136**, B864–B871, https://doi.org/10.1103/PhysRev.136.B864 (1964).
44. Kresse, G. & Furthmuller, J. Efficient Iterative Schemes for Ab Initio Total-Energy Calculations Using a Plane-Wave Basis Set. *Phys. Rev. B* **54**, 11169–11186, https://doi.org/10.1103/PhysRevB.54.11169 (1996).
45. Perdew, J. P., Burke, K. & Ernzerhof, M. Generalized Gradient Approximation Made Simple. *Phys. Rev. Lett.* **77**, 3865–3868, https://doi.org/10.1103/PhysRevLett.77.3865 (1996).
46. Yang, K. S., Dai, Y., Huang, B. & Feng, Y. P. First-Principles GGA Plus U Study of the Different Conducting Properties in Pentavalent-Ion-Doped Anatase and Rutile TiO_2. *J. Phys. D: Appl. Phys.* **47**, 275101, https://doi.org/10.1088/0022-3727/47/27/275101 (2014).
47. Pentcheva, R. & Pickett, W. E. Ionic Relaxation Contribution to the Electronic Reconstruction at n-Type $LaAlO_3$/$SrTiO_3$ Interface. *Phys. Rev. B* **78**, https://doi.org/10.1103/PhysRevB.78.205106 (2008).

Acknowledgements

This work was supported by the National Natural Science Foundation of China (Grants No. 51672171, 11274222, 11547011), the National Key Basic Research Program of China (Grant No. 2015CB921600), the Eastern Scholar Program from the Shanghai Municipal Education Commission, and the fund of the State Key Laboratory of Solidification Processing in NWPU (SKLSP201703). Special Program for Applied Research on Super Computation of the NSFC-Guangdong Joint Fund (the second phase), the supercomputing services from AM-HPC, the China Postdoctoral Science Foundation and the Fok Ying Tung Education Foundation are also acknowledged.

Author Contributions

C.C. and W.R. designed the research project; L.F. and J.Z. helped with literature search and writing; G.Z. carried out some theoretical analysis; C.C. carried out the calculations and drafted the manuscript; W.R. and J.Z. revised and finalized the manuscript; All authors reviewed the manuscript.

Additional Information

Supplementary information accompanies this paper at https://doi.org/10.1038/s41598-017-18858-x.

Competing Interests: The authors declare that they have no competing interests.

Publisher's note: Springer Nature remains neutral with regard to jurisdictional claims in published maps and institutional affiliations.